Journal of Magnetic Resonance 210 (2011) 98–106

Contents lists available at ScienceDirect

Journal of Magnetic Resonance

journal homepage: www.elsevier.com/locate/jmr

Slice with angulated non-parallel boundaries

BuSik Park [a,*], Martin J. Lizak [b], Yun Xiang [a], Jun Shen [a]

[a] Molecular Imaging Branch, National Institute of Mental Health Intramural Research Program, NIH, Bethesda, MD, USA
[b] Mouse Imaging Facility, National Institute of Neurological Disorders and Stroke, National Institutes of Health, Bethesda, USA

ARTICLE INFO

Article history:
Received 15 November 2010
Revised 15 February 2011
Available online 18 February 2011

Keywords:
Adiabatic pulse
Non-rectangular volume selection
Time-varying gradient

ABSTRACT

Adiabatic pulses are widely used for spatial localization in magnetic resonance spectroscopy because of their high immunity to RF inhomogeneity and excellent slice profiles. Since non-rectangular volume is often preferred in localized spectroscopy, we propose a scheme for selecting a trapezoidal slice using adiabatic π pulses. In this scheme, a time-varying gradient orthogonal to a stationary slice selection gradient is used to change the boundaries of the slice profile from parallel to non-parallel. Numerical simulation results for the transverse and longitudinal magnetization using different RF and gradient waveforms are presented for non-parallel slice selection. Phantom imaging and *in vivo* ^{1}H MRS of rat brain using non-parallel slices are demonstrated.

Published by Elsevier Inc.

1. Introduction

Magnetic resonance spectroscopy (MRS) can provide valuable information related to metabolism and function for clinical diagnosis and life science research. However, MRS is very sensitive to spurious interferences, for example, brain MRS can be contaminated by unwanted lipid signals from the scalp and retro-orbital spaces, which overlap with many metabolite resonances such as lactate, glutamate and N-acetyl aspartate (NAA) [1]. Therefore, it is essential to minimize signal contamination from outside the region of interest (ROI). Various ingenious spatial localization techniques including stimulated echo acquisition mode (STEAM) [2], point resolved spectroscopy (PRESS) [3] and image selected *in vivo* spectroscopy (ISIS) [4], have been developed for this purpose. These methods have been routinely used to select a cubic or rectangular ROI to extract localized spectroscopic information.

There has been a long-standing interest in the MRS field to develop the capability to select spectroscopic signals from non-rectangular volumes because it is difficult to place a sizable rectangular box in many anatomical structures (e.g., the hippocampus in the brain) without incurring a large partial volume effect. One of the desirable goals of spatial localization is to extract signals from irregularly shaped volumes of interest such that the boundary of the selected volume matches that of the intended anatomical structure. One technique, spectral localization by imaging (SLIM, [5]), addresses this issue by dividing a large volume into several irregularly shaped compartments based on high resolution anatomical images and assumes that each compartment has a spatially uniform spectrum. Spectra of these compartments may be resolved from data collected with a small number of phase encoding steps to differentiate signals originated from different compartments. Extraction of localized spectra from irregularly shaped compartments can also be achieved using sensitivity heterogeneity of multichannel receive coils [6]. By simultaneously modulating RF amplitude and gradient waveforms irregularly shaped volumes can also be selectively excited based on a *k*-space interpretation of small-flip-angle spatial excitation [7]. This *k*-space-based excitation method has recently been extended using radial *k*-space trajectories for improved spatial accuracy [8] or parallel RF transmission to shorten the duration of the RF pulses used for multidimensional excitation [9]. Non-rectangular volume selection may also be useful for outer volume suppression in chemical shift imaging because of the complexity of the shapes of tissues. For example, in proton chemical shift imaging of brain, usually six or eight slabs are used to suppress the lipid signal of the scalp [10].

It is well-known in the NMR literature that a pair of identical arbitrarily formulated 180° pulses achieve pure phase refocusing at the 2nd echo [11]. This principle has been used to select rectangular volumes using three pair of adiabatic full passage pulses (AFP) [12]. Recently, Sacolick et al. demonstrated that single AFP pulses applied along non-equivalent spatial axes can achieve significant phase refocusing [13]. When the phase across a spectroscopic voxel is small, the remaining nonlinear phase of the AFP pulses becomes inconsequential. As such rectangular and octagonal volumes can be selected for proton chemical shift imaging while halving the number of AFP pulses required.

In this work we propose a new method for selecting non-rectangular volumes for localized spectroscopy by adding a time-varying gradient [14] orthogonal to the conventional slice selection

* Corresponding author. Address: Molecular Imaging Branch, National Institute of Mental Health, Bldg. 10, Rm. 2D 50, 9000 Rockville Pike, Bethesda, MD 20892-1527, USA. Fax: +1 301 480 2395.
E-mail address: parkb3@mail.nih.gov (B. Park).

1090-7807/$ - see front matter Published by Elsevier Inc.
doi:10.1016/j.jmr.2011.02.016

gradient. We first gave a theoretical description of the proposed method and then verified it using Bloch simulation. Several RF and gradient waveforms were evaluated numerically and experimentally. *In vivo* MR spectroscopy of rat brain acquired from a trapezoidal volume using the proposed method is also demonstrated.

1.1. Theory

For an effective adiabatic sweep, the magnetization as a function of position and time follows the trajectory of the effective field (B_{1eff}) as originally described by Baum et al. [15]. That is, the polar and azimuthal angles of the magnetization can be accurately approximated by those of the B_{1eff}. As a result, the equation of motion for the longitudinal magnetization M_Z as a function of position ($\mathbf{r}$) and time (t) can be described by

$$M_Z(\gamma\mathbf{G}(t)\cdot\mathbf{r}+\Delta\omega_0,t)=(\gamma\mathbf{G}(t)\cdot\mathbf{r}+\Delta\omega_0-\omega(t))/(A^2(t)+(\gamma\mathbf{G}(t)\cdot\mathbf{r}+\Delta\omega_0-\omega(t))^2)^{0.5} \quad (1)$$

where $\mathbf{G}(t)$ is the time-varying gradient vector modulation function, $\Delta\omega_0$ is the carrier frequency offset that determines the position of the slice center, $A(t)$ and $\omega(t)$ are the amplitude and angular frequency modulation functions of the adiabatic pulse, respectively. For spins located at slice center $M_Z(t) = -\omega(t)/(A^2(t) + (-\omega(t))^2)^{0.5}$. At the slice boundaries, the adiabatic condition breaks down. Eq. (1) becomes an indeterminate (0/0). That is, at slice boundaries, we have

$$\gamma\mathbf{G}(t)\cdot\mathbf{r}+\Delta\omega_0-\omega(t)=0 \quad (2)$$

Note that the slice boundaries are formed when $\omega(t)\approx\gamma\mathbf{G}(t)\cdot\mathbf{r}+\Delta\omega_0$ while the RF pulse has little influence over slice boundaries when $\omega(t)\gg\gamma\mathbf{G}(t)\cdot\mathbf{r}+\Delta\omega_0$ or $\omega(t)\ll\gamma\mathbf{G}(t)\cdot\mathbf{r}+\Delta\omega_0$. Therefore, for sufficiently long slice-forming time intervals (i.e., $|\omega(t)| = \omega_0$), if $\mathbf{G}(0 < t \ll T_P)\approx\mathbf{G}(0)$, $\mathbf{G}(0 \ll t < T_P)\approx\mathbf{G}(T_P)$ and assuming that the stationary and time-varying gradients are applied along Z and Y axes, respectively, we have

$$Z(0)=-G_Y(0)/G_Z\times Y(0)-(\Delta\omega_0+\omega_0)/\gamma G_Z \quad (3)$$

and

$$Z(T_P)=-G_Y(T_P)/G_Z\times Y(T_P)-(\Delta\omega_0-\omega_0)/\gamma G_Z \quad (4)$$

where T_p is the duration of the pulse, $\mathbf{r}(0)$ and $\mathbf{r}(T_P)$ denote slice boundaries. A direct consequence of Eqs. (3) and (4) is that the slice angle (ϕ_{slice}) and gradient angle ($\phi_{gradient}$) are approximately equal for RF and gradient modulation functions that allow formation of slice boundaries under approximately constant $\mathbf{G}(t)$.

2. Materials and methods

Numerical calculations were performed to simulate the *XY*-(transverse) and *Z*-(longitudinal) magnetizations with a variety of time-varying gradient and RF waveforms. To validate the numerical calculations, experimental measurements using a cylindrical water phantom and young adult rats ($n = 3$) were performed.

All simulation work was performed using in-house MATLAB (The MathWorks, Inc., Natick, MA, USA) programs for solving Bloch equations without the relaxation terms. These programs were used to compute transverse and longitudinal components of magnetization generated by an AFP pulse, a constant *Z*-gradient and a time-varying *Y*-gradient. An example of this scheme is shown in Fig. 1 where a linearly time-varying anti-symmetric *Y* gradient is added to a stationary *Z*-gradient during the execution of an AFP pulse with a pulse length of T_p. Several different RF and time-varying gradient shapes including linear, arctan, and hyperbolic tangent (tanh) were evaluated. The results for the hyperbolic secant RF pulse ($(A(t) = \mu\beta\mathrm{sech}(\beta_{0.5} - t/T_P))$; $\omega(t) = \mu\beta\tanh(\beta_{0.5} - t/T_p))$; $\beta T_p = 2\ln(200)$)) were shown. The angle between the two slice

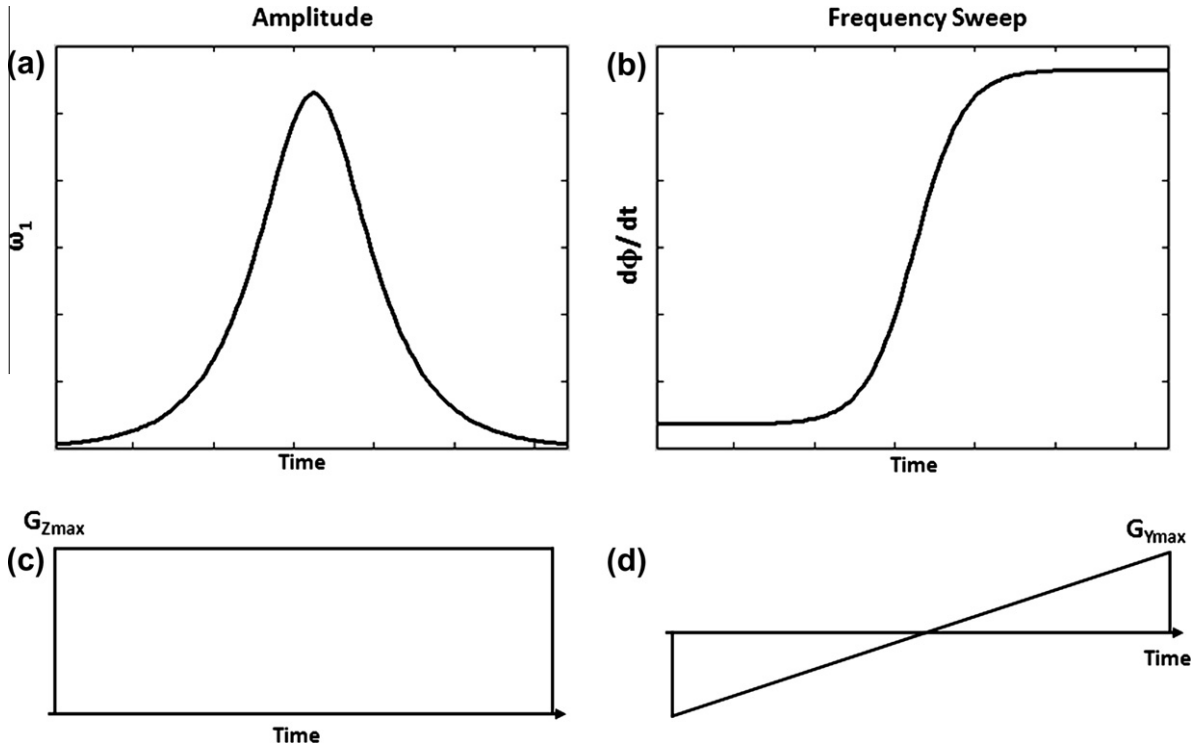

Fig. 1. A proposed scheme for generating non-parallel inversion slice. RF pulse amplitude ω_1 (a), frequency sweep $d\phi/dt$ (b), and gradient waveforms of Z (c) and Y (d) directions. A standard hyperbolic secant (sech) RF pulse was used without any modification. Pulse duration (T_P) = 2 ms, truncation level = 1%, $\gamma B_1 = 0.5\times$ frequency sweep width, $\mu = 5.0$, $G_Z = 47.0$ and $G_{Ymax} = 9.4$ mT/m.

boundaries calculated by Bloch simulation (ϕ_{slice}) were compared with the angle between the initial and final gradient vectors ($\phi_{gradient} = |\arctan(G_Y(t=0)/G_Z) - \arctan(G_Y(t=T_p)/G_Z)|$).

Experimental measurements were performed using a Bruker AVANCE spectrometer (Bruker Biospin, Billerica, MA, USA) interfaced to an 11.7 T (500.14 MHz) 89-mm inner diameter (ID) vertical bore magnet (Magnex Scientific, Abingdon, UK), and a 56 mm ID water-cooled Mini0.5 gradient coil with a maximum gradient strength of 3 G/mm and rise time of 100 μs (Bruker Biospin, Billerica, MA, USA). A home-built one loop surface RF transmit and receive coil with a 15 mm ID integrated into an animal handling system [16] containing a head-holder (including a bite bar and ear pins) was used. Usage of the rats was approved by the National Institute of Mental Health Animal Care and Use Committee. For the *in vivo* MR spectroscopy experiment, the rat brain was shimmed using the FLATNESS (Five Linear Acquisitions for up to Third order Noniterative, Efficient Slice Shimming) automatic slice shimming method [17] by mapping along projections to correct the first, second and third order in-slice and through slice B_0 inhomogeneity terms [18].

3. Results

Fig. 2 shows the results of numerical simulations using the RF and gradient scheme shown in Fig. 1 over a two-dimensional sample space (20×20 mm^2). The well-known hyperbolic secant pulse was used without any modification. Pulse duration (T_p) = 2 ms, truncation level = 1%, $\gamma B_1 = 0.5 \times$ frequency sweep width, $\mu = 5.0$, $G_Z = 47.0$ mT/m, $G_{Y\max} = 0$, 4.7, 9.4 mT/m, where μ is the adiabaticity factor and G_Y is the time-varying gradient. Fig. 2a and b shows calculated M_{XY} and M_Z magnetizations with $G_Y = 0$. Fig. 2c–f shows the calculated M_{XY} and M_Z magnetizations with $G_Y = G_{Y\max}(2t/T_p - 1)$ when $0 \leqslant t \leqslant T_p$. As shown by Fig. 2c–f, non-parallel trapezoidal slice profiles were produced for $G_{Y\max} \neq 0$. Based on Bloch simulation the gradient angles ($\phi_{gradient}$) are 11.4° and 22.6°, whereas the slice angles are 5.0° and 10°corresponding to a $G_{Y\max}$ of 4.7 and 9.4 mT/m (see Table 1), respectively. As shown in Fig. 2, the width of transition bands for off-centered magnetization increased as $G_{Y\max}$ was increased from 0 to 9.4 mT/m.

Fig. 3 shows that asymmetric G_Y gradient waveforms can be used to generate asymmetric non-parallel slices. In Fig. 3a, $G_Y = G_{Y0}(0.5 - 2t/T_p)$. $G_{Y0} = 9.4$ mT/m. Noticeably, although a non-zero G_Y gradient was applied at $t = 0$, the initial slice boundary of the excited slice is found to be perpendicular to the Z axis. In Fig. 3b, $G_Y = G_{Y0}(2 - 2t/T_p)$. In Fig. 3c, $G_Y = G_{Y0}(2t/T_p)$ when $0 \leqslant t \leqslant T_p$. In the latter two cases, the slice boundary corresponding to $G_Y = 0$ is not perpendicular to the Z axis. Calculated slice and gradient angles are shown in Table 2.

Fig. 4 compares three different G_Y waveforms. In Fig. 4a, the linear waveform depicted in Fig. 1 was used with $G_{Y\max} = 4.7$ mT/m. The middle panel shows the two-dimensional map of the

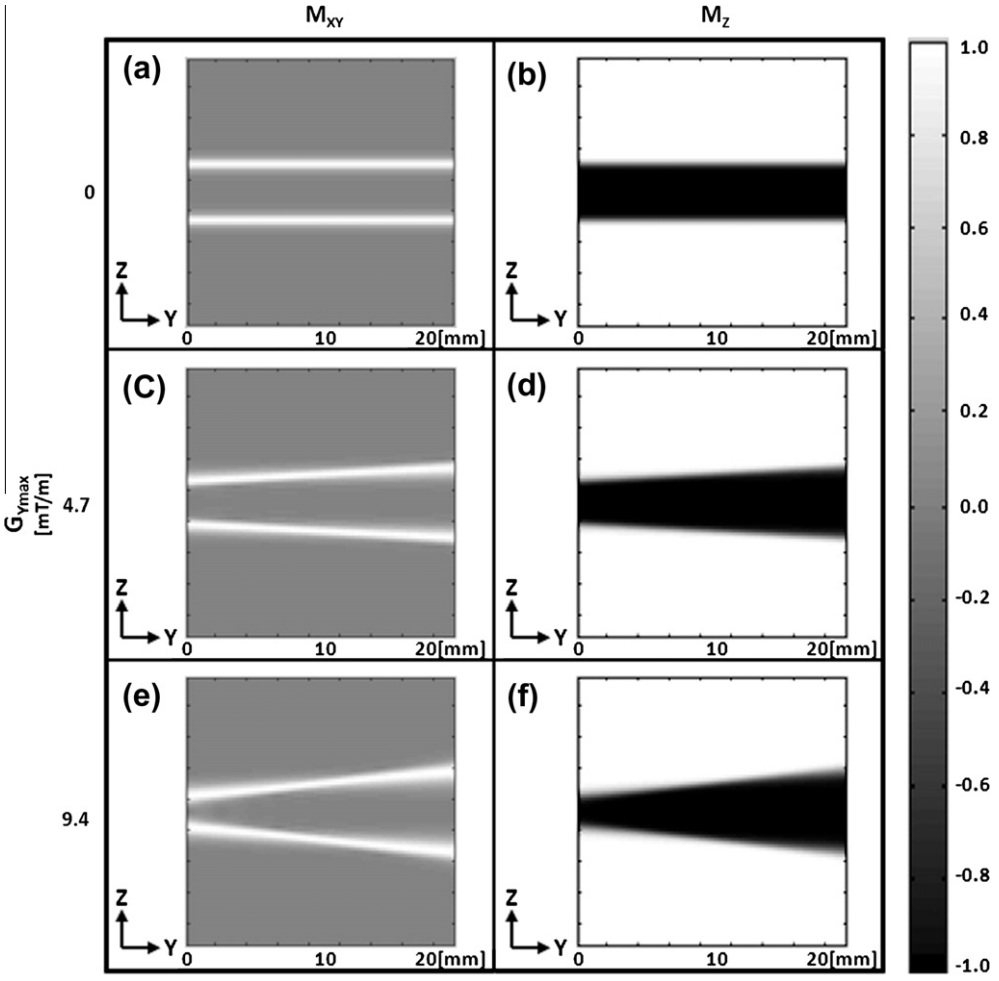

Fig. 2. Numerical simulation results of the *XY*-(first column) and *Z*-(second column) magnetization with different maximum *Y*-gradient strength ($G_{Y\max}$) of 0 (a and b), 4.7 (c and d), and 9.4 (e and f) [mT/m]. Other parameters of RF and *Z*-gradient waveforms are the same as in Fig. 1. The displayed image size is 20×20 mm^2.

Table 1
Gradient and slice angles in Fig. 2 corresponding to the maximum *Y*-gradient amplitudes of 4.7 and 9.4 mT/m. *Z*-gradient amplitude = 47.0 mT/m. The hyperbolic sequent pulse in Fig. 1 is used for RF excitation. The difference between gradient and slice angles were calculated using difference = $(\phi_{gradient} - \phi_{slice})/\phi_{gradient} \times 100$ (%).

G_{Ymax} (mT/m)	4.7	9.4
$\phi_{gradient}$ (°)	11.4	22.6
ϕ_{slice} (°)	5.0	10.0
Difference (%)	56.1	55.8

Table 2
Gradient and slice angles of the selected region in Fig. 3. G_{Y0} = 9.4 mT/m. Other RF and *Z*-gradient waveforms are the same as in Table 1.

	Top (a)	Middle (b)	Bottom (c)
Start $\phi_{gradient}$ (°)	−5.7	−21.8	0
End $\phi_{gradient}$ (°)	16.7	0	21.8
Total $\phi_{gradient}$ (°)	21.8	21.8	21.8
Start ϕ_{slice} (°)	0	15.5	5.5
End ϕ_{slice} (°)	−10.0	5.5	15.5
Total ϕ_{slice} (°)	10.0	10.0	10.0
Difference in total angle (%)	54.1	54.1	54.1

simulated residual transverse magnetization M_{XY}. The inversion bands shown in the right panel correspond to the three colored arrows in the middle panel. A progressively broadening of the inversion bands is seen as the *Y* ordinate is moved from left to right. In Fig. 4b, an arctan (truncation level = 1%) G_Y waveform was applied with the same G_{Ymax}. A marked narrowing of the transition bands for off-centered magnetization was observed. A further improvement was seen in Fig. 4c where a hyperbolic tangent (tanh, truncation level = 1%) G_Y waveform was used to produce the time-varying *Y*-gradient waveform. The gradient angle is 21.8° for all three waveforms, whereas the slice angles are 10.0°, 20.0°, and 22.0°, corresponding to linear, arctan and tanh gradient waveforms (see Table 3). Of all the *Y*-gradient waveforms evaluated in Figs. 1–4, the hyperbolic tangent waveform produced the smallest difference between gradient and slice angles.

Fig. 5 shows the effect of increasing the gradient angle on the slice profile using the tanh *Y*-gradient waveform. Similar to the results given in Fig. 2, the slice angle varies linearly with the gradient angle when the perturbation in the *Y* direction is not large. Our simulation showed that this linearity holds well for $G_{Ymax}/G_Z < 0.15$. The gradient and slice angles corresponding to G_{Ymax} = 9.4, 14.1 and 18.8 mT/m are listed in Table 4. The discrepancy between gradient and slice angles increases with increasing G_{Ymax}/G_Z ratios.

The above theoretical and numerical simulation results show that schemes similar to that depicted in Fig. 1 can generate non-parallel slice profiles. As a first experimental test, we performed one-dimensional (1D) spin echo imaging experiments on a

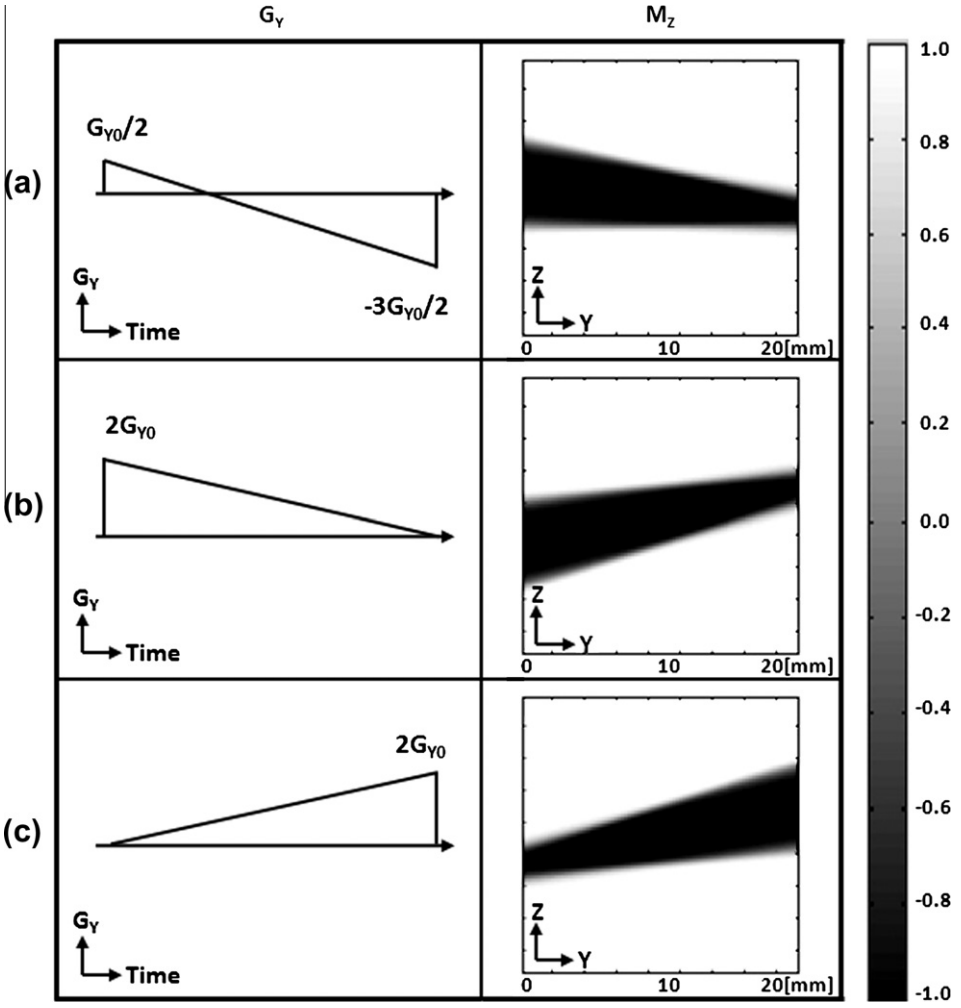

Fig. 3. Numerical simulation results of the *Z*-magnetization (second column) with different linear *Y*-gradient waveforms (G_{Y0} = 9.4 mT/m). Parameters of RF and *Z*-gradient waveforms are the same as in Fig. 1. (a) $G_Y = G_{Y0}(0.5 - 2t/T_p)$. (b) $G_Y = G_{Y0}(2 - 2t/T_p)$. (c) $G_Y = G_{Y0}(2t/T_p)$ when $0 \leqslant t \leqslant T_p$. The displayed image size is 20×20 mm^2.

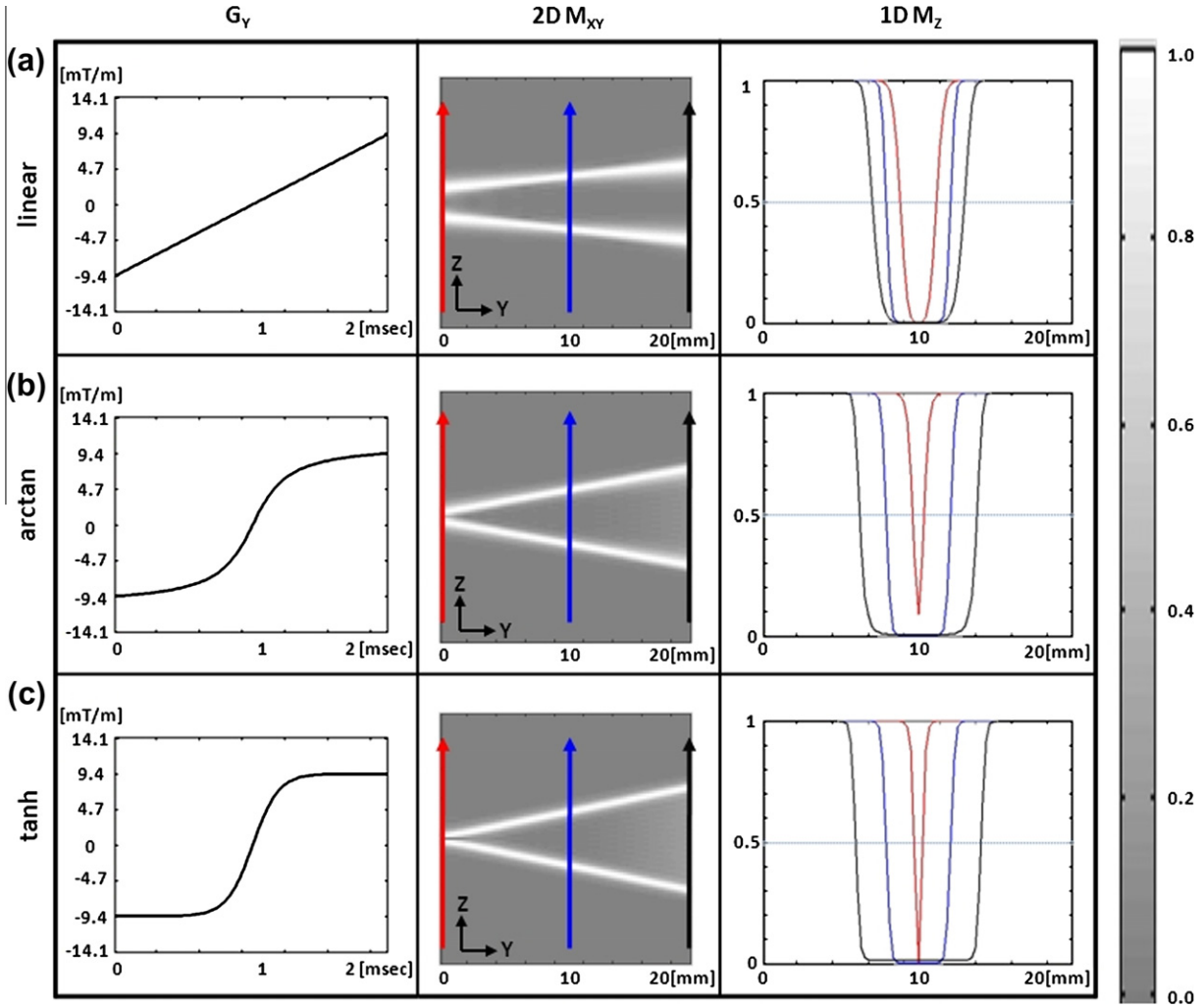

Fig. 4. Comparison of three different G_Y waveforms. (a) Linear waveform as depicted in Fig. 1 with $G_{Y\max}$ = 9.4 mT/m. The middle panel shows the 2D map of the simulated residual transverse magnetization M_{XY}. The cross-sectional profile of the inversion bands was shown in the right panel. The color of the cross-sectional profiles of the inversion bands corresponds to the color of arrow in the 2D map which marks the *Y* ordinate of the cross-sectional profile. (b) arctan G_Y waveform with $G_{Y\max}$ = 9.4 mT/m. (c) Hyperbolic tangent (tanh) G_Y waveform with $G_{Y\max}$ = 9.4 mT/m. The displayed image size is 20 × 20 mm^2.

Table 3
Gradient and slice angles of the selected region in Fig. 4 corresponding to linear, arctan and tanh *Y*-gradient waveforms with the same RF and gradient parameters as in Table 2.

G_{Y0}	Linear	arctan	tanh
$\phi_{gradient}$ (°)	21.8	21.8	21.8
ϕ_{slice} (°)	10.0	20.0	22.0
Difference (%)	54.1	8.3	1.0

cylindrical water phantom. The pulse sequences (Fig. 6a and c) were programmed using Paravision 3.0.1 (Bruker Biospin, Billerica, MA, USA). A non-selective 90° rectangular pulse was used for excitation. A pair of two identical 2-ms adiabatic sech 180° RF pulses (truncation level = 1%, μ = 5.0) were used for slice selective pure phase refocusing. The stationary slice selection gradient was placed on the spatial *Z* axis (G_Z = 59.9 mT/m). The projection of the *Z* slice on the spatial *Z* axis was measured (TR/TE = 3090/28.7 ms, field-of-view (FOV) = 40 mm, data size = 512, and number of average = 1). The 1D image was shown in Fig. 6b. Upon adding a nonzero time-varying hyperbolic tangent *Y* gradients (tanh, 1% truncation), the vertical boundaries of the 1D image becomes non-parallel. The 1D image for $G_{Y\max}$ = 15.0 mT/m is shown in Fig. 6d. $\phi_{gradient}$ = 26.6°, the simulated ϕ_{slice} = 27.0°. Since the projection of a trapezoidal *Z* slice of uniform magnetization onto the *Z* axis (1D *Z* image) is similar to the slice profile the results in Fig. 6d suggest that a non-parallel slice is generated as expected.

To further visualize the action of time-varying *Y* gradients, 2D spin echo imaging experiments were performed on the cylindrical water phantom. The spin echo pulse sequence was similar to those depicted in Fig. 6a and c except that phase encoding gradients were added to generate *YZ* images of the selected *Z* slice. TR/TE = 600/30.7 ms, FOV = 40 × 40 mm^2, matrix size = 256 × 256, number of average = 1. Fig. 7a shows the *YZ* image of the cylindrical water phantom which is typical for that generated by a surface transceiver coil. In Fig. 7b, T_p = 2 ms, truncation level = 1%, μ = 5.0, $G_{Y\max}$ = 21.0 mT/m, G_Z = 59.9 mT/m, $\phi_{gradient}$ = 35.0°, ϕ_{slice} from Bloch simulation = 37.5°, and ϕ_{slice} measured from the image acquired experimentally ≈39.5°.

Fig. 8 shows results of *in vivo* ^{1}H MR spectroscopy of rat brain with a conventional rectangular ROI and a trapezoidal ROI. A spin echo coronal anatomical image was shown in Fig. 8a. TR/TE = 3000/11.6 ms, FOV = 20 × 20 mm^2, slice thickness = 1 mm, matrix size = 128 × 128, number of average = 1. The *in vivo* MRS experiment with a rectangular ROI was performed after a fully automatic FLATNESS shimming procedure [17]. The single-shot adiabatic 3D

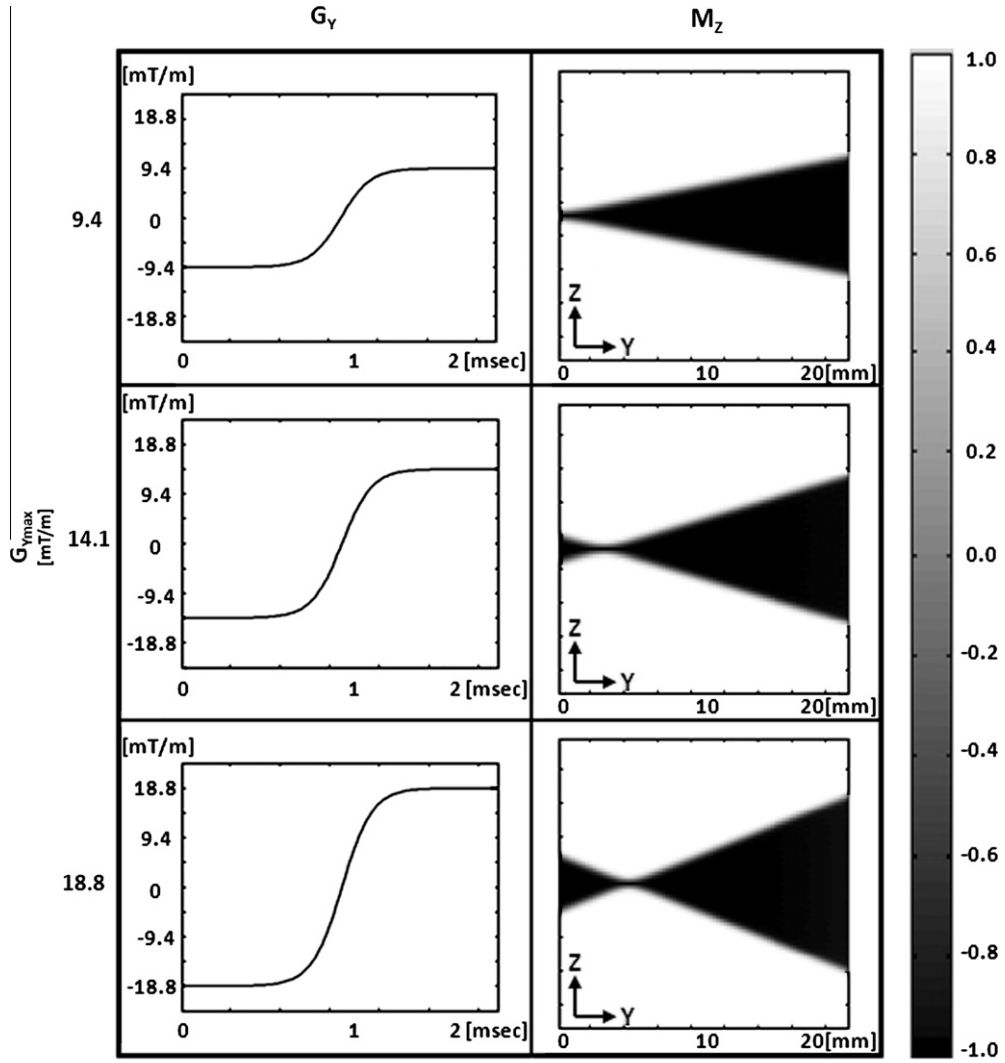

Fig. 5. Numerical calculation results of the *Z*-magnetization (second column) with different $G_{Y\max}$ for a hyperbolic tangent *Y*-gradient waveform. Other parameters of RF and *Z*-gradient waveforms are the same as in Fig. 1. (a) $G_{Y\max}$ = 9.4 mT/m. (b) $G_{Y\max}$ = 14.1 mT/m. (c) $G_{Y\max}$ = 18.8 mT/m. The displayed image size is 20 × 20 mm^2.

Table 4
Gradient and slice angles of the selected region in Fig. 5 for different $G_{Y\max}$ values. Other parameters are the same as in Table 2.

$G_{Y\max}$ (mT/m)	9.4	14.1	18.8
$\phi_{gradient}$ (°)	21.8	31.0	38.7
ϕ_{slice} (°)	22.0	33.0	43.0
Difference (%)	1.0	6.5	11.1

localization pulse sequence [12] used a non-selective adiabatic half passage pulse (1 ms) for excitation and three pairs of identical AFP pulses (2-ms sech pulses, μ = 5.0, truncation level = 1%) for slice selection. TR/TE = 1000/18 ms, VOI = 4 × 2 × 4 mm^3, Number of average = 512, and data size = 4096. Repeated CHESS pulses were used for water suppression [19]. Orthogonal gradient pairs or triplets carefully adjusted to minimize the residual B_0 shifts were used as crushers for CHESS water suppression, outer volume suppression and for the six slice-selective refocusing AFP pulses. The acquired localized MR spectrum was shown in Fig. 8b. To generate a trapezoidal ROI, the slice selection gradients for the *Y* slice were modified by adding a pair of simultaneous hyperbolic tangent *X* gradients. $G_{X\max}/G_Y$ = 0.25 (G_Y = 59.9 mT/m, $G_{X\max}$ = 15.0 mT/m, same as Fig. 6). The corresponding MR spectrum was shown in Fig. 8c. In both Fig. 8b and c, high quality ^{1}H MR spectra of the rat brain were obtained. These spectra are similar to those previously published by our laboratory [19].

4. Discussion

Our results showed that slices with non-parallel boundaries can be generated by changing the initial and final direction of the slice gradient vector for adiabatic frequency sweep. Using a single AFP pulse, this scheme can generate inversion slice with non-parallel boundaries. When this scheme is repeated for pure phase refocusing [20], it can be easily incorporated into the adiabatic PRESS method [12] for localized spectroscopy as demonstrated by the results shown in Fig. 8.

We found large differences between gradient and slice angles when orthogonal linear time-varying gradients are used to introduce the nonparallelness (see Tables 1–3). Interestingly, with linear time-varying gradients a nonzero start or end gradient amplitude (Fig. 3a) is needed such that the corresponding slice boundary remains perpendicular to the slice gradient direction. When the start or end amplitude of the perturbing gradient is zero, the corresponding slice boundary is no longer perpendicular to the slice gradient direction (Fig. 3b and c). It should be noted that the

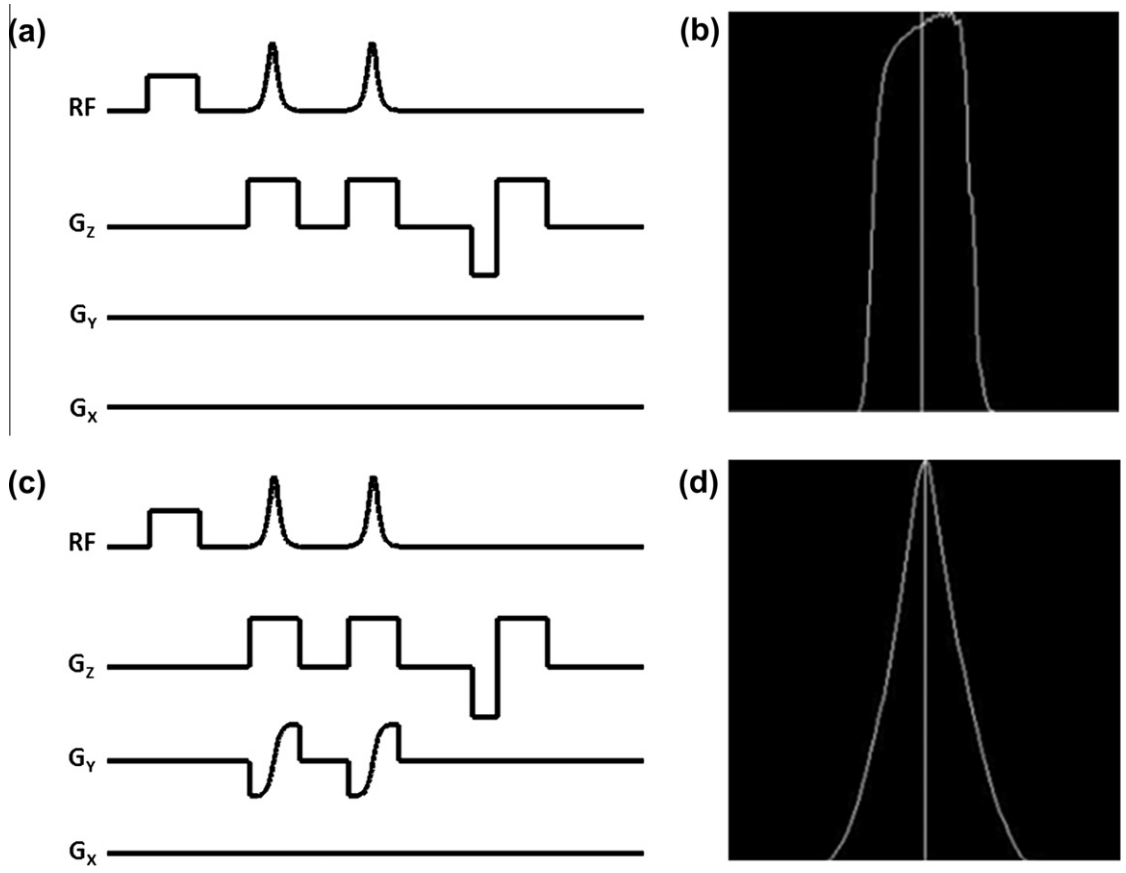

Fig. 6. Schematic drawing of pulse sequences (a and c) and experimentally acquired 1D image (b and d) using a cylindrical phantom of water. A non-selective 90° rectangular pulse was used for excitation. A pair of two identical 2-ms adiabatic sech 180° RF pulses (truncation level = 1%, μ = 5.0) were used for slice selective pure phase refocusing (a and c). The stationary slice selection gradient was placed on the spatial Z axis (59.9 mT/m). Time-varying hyperbolic tangent Y gradients ($G_{Y\max}$ = 15.0 mT/m) were used to generate non-parallel slice boundaries (c and d). Crusher gradients were not drawn for clarity. TR/TE = 3090/28.7 ms, field-of-view (FOV) = 40 mm, data size = 512, and number of average = 1.

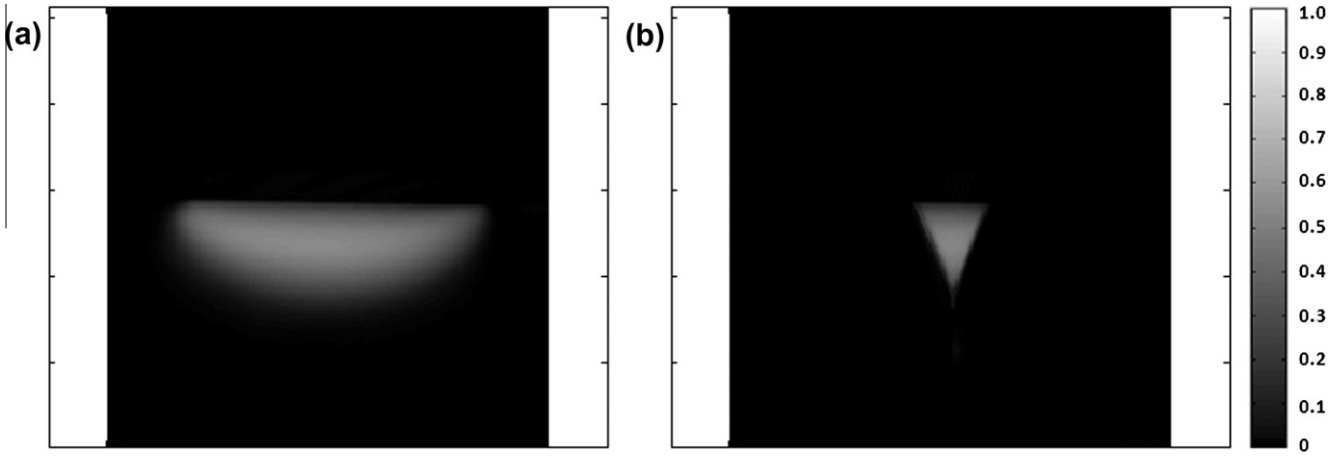

Fig. 7. Experimentally acquired 2D phantom image without (a) and with (b) a time-varying hyperbolic tangent gradient using a cylindrical phantom of water and a single loop coil to transmit and receive signal. TR/TE = 600/30.7 ms, FOV = 40 × 40 mm, matrix size = 256 × 256, number of average = 1, T_p = 2 ms, truncation level = 1%, μ = 5.0, $G_{Y\max}$ = 0 or 21.0 mT/m, G_Z = 59.9 mT/m. (a) YZ image of the cylindrical water phantom with $G_{Y\max}$ = 0. (b) YZ image of the cylindrical water phantom with $G_{Y\max}$ = 21.0 mT/m. Slice angle from Bloch simulation is 37.5° and gradient angle of 35.0°. The measured slice angle from the image acquired experimentally is about 39.5°.

start gradient angle at the infinitesimal t = 0 cannot completely determine the start slice angle, the latter requires a finite time interval to allow the frequency of the AFP pulse to sweep sufficiently away from the slice boundary. Similar analysis also applies to the end slice angle. Therefore the gradient vector direction during a significant portion of the initial and final periods of the AFP pulse influences the slice angle. With linear time-varying perturbation, the gradient angle is progressively reduced from $G_Y(0)$ during the initial period of the pulse. Based on the above analysis one expects that the start slice angle is smaller than the corresponding

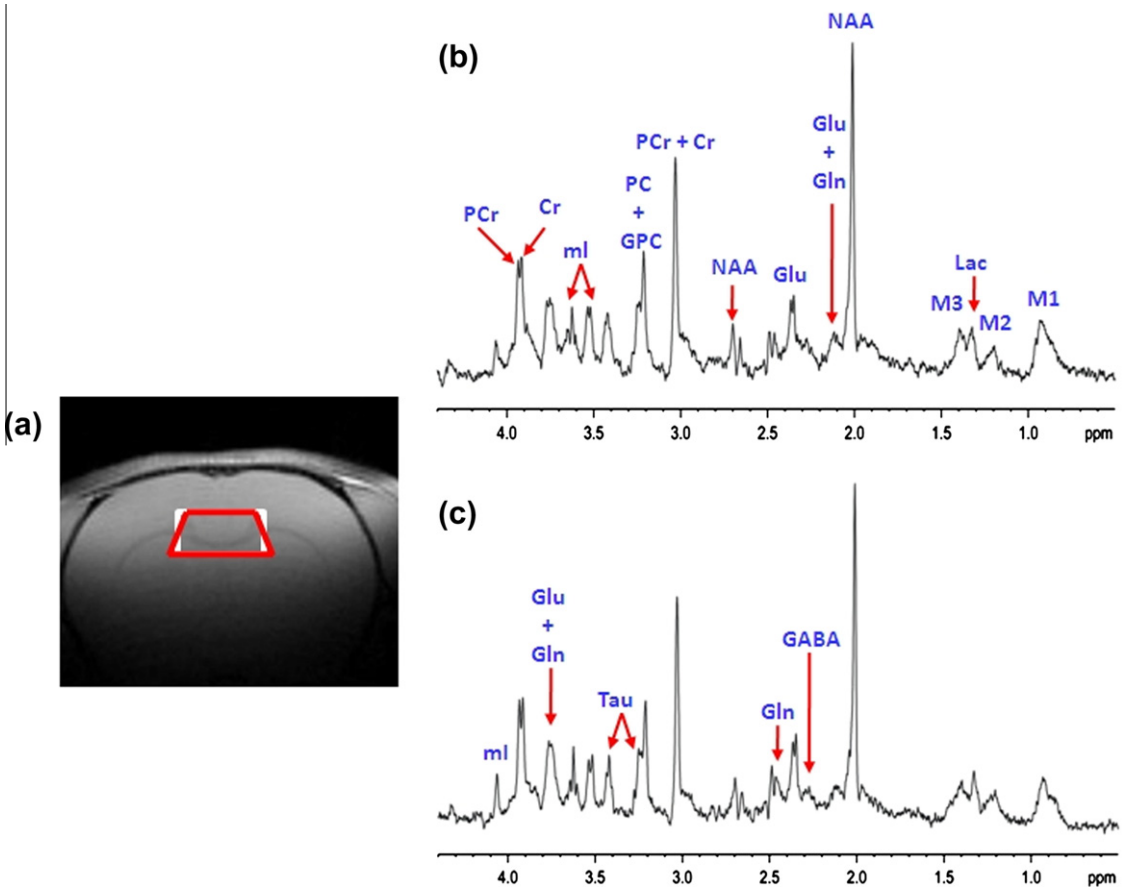

Fig. 8. (a) Spin echo coronal anatomical image. TR/TE = 3000/11.6 ms, FOV = 20 × 20 mm^2, slice thickness = 1 mm, matrix size = 128 × 128, number of average = 1. Two ROIs are displayed in (a) with white (rectangle) and red (trapezoid) color. (b) Localized *in vivo* proton MR spectra acquired at 11.7 T from a rectangular ROI in the rat brain. TR/TE = 1000/18 ms, VOI = 4 × 2 × 4 mm^3, Number of average = 512. (c) Localized *in vivo* proton MRS spectra acquired at 11.7 T from a trapezoidal ROI in the rat brain. To generate a trapezoidal ROI, the slice selection gradients for the *Y* slice were modified by adding a pair of simultaneous hyperbolic tangent *X* gradients. $G_{X\max}/G_Y = 0.25$. Cr = creatine, GABA = γ-aminobutyric acid, Gln = glutamine, Glu = glutamate, GPC = glycerophosphocholine, Lac = lactate, M1, 2, 3 = macromolecule at 0.92, 1.21 and 1.39 ppm, mI = myo-inositol, NAA = N-acetylaspartate, PC = phosphocholine, PCr = phosphocreatine, Tau = taurine.

gradient angle for a linear gradient waveform. The same is also true for the final slice angle.

Thus, to minimize the difference between slice and gradient angles the perturbing gradient should have approximately constant amplitude during the initial and final portion of the AFP pulse as described in Theory. Based on this insight we investigated arctan and tanh waveforms. The results shown in Fig. 4 and Table 3 are in agreement with our analysis. The tanh waveform, which showed the least variation of G_Y during a significant portion of the initial and final periods of the AFP pulse, generates the smallest difference between gradient and slice angles.

The perturbing gradient, however, also degrades the adiabaticity of the AFP pulse. We expect, therefore, that one cannot generate very large slice angles using our method. As shown by Table 4, the deviation between gradient and slice angles also increases with $G_{Y\max}/G_Z$. Larger angles, as the XY angles depicted in Fig. 8a, can be generated between different slices, however.

A necessary condition for the proposed method to generate angulated, non-parallel slices is that the RF pulse has to fulfill the adiabatic requirements [15]. In addition to the AFP sech pulses, we also investigated other AFP pulses such as the adiabatic gauss, Lorentzian and cos^2 pulses [21] and modified chirp pulses [18] with similar results. In all cases investigated here existing AFP pulses were used. Optimization of frequency sweep to improve the adiabaticity of the pulse during rapid gradient modulation is expected to further improve the performance of our method. We will address the optimization issue in future work. In this work we have attempted to match the slice angles with the gradient angles. The significance of achieving equality between gradient and slice angles is for prescribing time-varying gradients in situ without resorting to Bloch simulations. It should also be pointed out that matching the two angles is not a requirement. Fig. 3 shows some examples of the diverse slice profiles one can generate using simple linear gradient waveform modulation. Many other non-parallel slice profiles can also be easily generated using the proposed strategy. The results in Fig. 8 showed that it is feasible to incorporate slice with angulated, non-parallel boundaries into localized spectroscopy sequences. It should also be possible to prescribe slice angles to match a specific anatomical structure in human brain studies.

Finally, our numerical simulations and experimental results showed that slices with angulated non-parallel boundaries can be generated using inversion of equilibrium magnetization or a double AFP spin echo of transverse magnetization [20,22]. Incorporating our method into other localization schemes that exploit frequency sweep and adiabatic pulses is also possible. For example, it can be used in the α–π adiabatic spin echo method [23] for canceling the second order phase across the slice generated by frequency sweep excitation [18]. The slice boundaries of the FOCI pulses [24,25] can also be modified similarly.

In conclusion, we demonstrate a novel scheme to directly generate slice with non-parallel boundaries. The performance of this

method may be further improved using sophisticated numerical optimization of both the RF and gradient waveforms. We expect that this method may find applications in many MRS as well as MRI applications where localizing a non-rectangular volume is of interest.

Acknowledgments

The authors thank Mr. Chris Johnson for helping with the *in vivo* spectroscopy experiments, and Dr. Steve Li, Dr. Yan Zhang, and Dr. Jan Willem van der Veen for helpful discussions. The authors also thank to the National Institutes of Health Fellows Editorial Board for the editorial assistance. This work is supported by the Intramural Research Program of the National Institutes of Health, National Institute of Mental Health.

References

[1] L. Kwock, M.A. Brown, M. Castillo, Extraneous lipid contamination in single-volume proton MR spectroscopy: phantom and human studies, AJNR 18 (1997) 1349–1357.
[2] J. Frahm, K.D. Merboldt, W. Hanicke, Localized proton spectroscopy using stimulated echoes, J. Magn. Reson. 72 (1987) 502–508.
[3] P.A. Bottomley, Spatial localization in NMR spectroscopy *in vivo*, Ann. N. Y. Acad. Sci. 508 (1987) 333–348.
[4] R.J. Ordidge, A. Connelly, J.A.B. Lohman, Image-selected *in vivo* spectroscopy (ISIS) – a new technique for spatially selective NMR-spectroscopy, J. Magn. Reson. 66 (1986) 283–294.
[5] X. Hu, D.N. Levin, P.C. Lauterbur, T. Spraggins, SLIM: spectral localization by imaging, Magn. Reson. Med. 8 (1988) 314–322.
[6] L. An, S. Warach, J. Shen, Spectral localization by imaging using multielement receiver coils, Magn. Reson. Med., in press. doi:10.1002/mrm.22783.
[7] J. Pauly, D. Nishimura, A. Macovski, A k-space analysis of small-tip-angle excitation, J. Magn. Reson. 81 (1989) 43–56.
[8] Q. Qin, J.C. Gore, M.D. Does, M.J. Avison, R.A. de Graaf, 2D arbitrary shape-selective excitation summed spectroscopy (ASSESS), Magn. Reson. Med. 58 (2007) 19–26.
[9] U. Katscher, P. Bornert, C. Leussler, J.S. van den Brink, Transmit SENSE, Magn. Reson. Med. 49 (2003) 144–150.
[10] D.C. Shungu, J.D. Glickson, Sensitivity and localization enhancement in multinuclear *in vivo* NMR spectroscopy by outer volume presaturation, Magn. Reson. Med. 30 (1993) 661–671.
[11] M.R. Bendall, R.E. Gordon, Depth and refocusing pulses designed for multi-pulse NMR with surface coils, J. Magn. Reson. 53 (1983) 365–385.
[12] J. Slotboom, W.M.M.J. Bovee, Adiabatic slice-selective RF pulses and a single-shot adiabatic localization pulse sequence, Concepts Magn. Reson. 7 (3) (1995) 93–217.
[13] L.I. Sacolick, D.L. Rothman, R.A. de Graaf, Adiabatic refocusing pulses for volume selection in magnetic resonance spectroscopic imaging, Magn. Reson. Med. 57 (2007) 548–553.
[14] S. Conolly, D. Nishimura, A. Macovski, Variable-rate selective excitation, Magn. Reson. Med. 78 (1988) 440–458.
[15] J. Baum, R. Tycko, A. Pines, Broadband population inversion by phase modulated pulses, J. Chem. Phys. 79 (9) (1983) 4643–4644.
[16] S. Li, J. Shen, Integrated RF probe for in vivo multinuclear spectroscopy and functional imaging of rat brain using an 11.7 Tesla 89 mm bore vertical microimager, MAGMA 18 (2005) 119–127.
[17] Z. Chen, S.S. Li, J. Yang, D. Letizia, J. Shen, Measurement and automatic correction of high-order B0 in-homogeneity in the rat brain at 11.7 Tesla, Magn. Reson. Imaging 22 (2004) 835–842.
[18] J. Shen, Y. Xiang, High fidelity magnetic resonance imaging by frequency sweep encoding and Fourier decoding, J. Magn. Reson. 204 (2010) 200–207.
[19] S. Xu, J. Yang, J. Shen, Measuring N-acetylaspartate synthesis *in vivo* using proton magnetic resonance spectroscopy, J. Neurosci. Methods 172 (2008) 8–12.
[20] T. Hwang, A.J. Shaka, Water suppression that works. Excitation sculpting using arbitrary waveforms and pulsed field gradients, J. Magn. Reson. A 112 (1995) 275–279.
[21] E. Kupce, R. Freeman, Optimized adiabatic pulses for wideband spin inversion, J. Magn. Reson. A 118 (1996) 299–303.
[22] M.H. Levitt, R. Freeman, Compensation for pulse imperfections in NMR spin-echo experiments, J. Magn. Reson. 43 (1981) 65–80.
[23] D. Kunz, Use of frequency-modulated radiofrequency pulses in MR imaging experiments, Magn. Reson. Med. 3 (1986) 377–384.
[24] J. Shen, Z. Chen, J. Yang, New FOCI pulses with reduced radiofrequency power requirements, J. Magn. Reson. Imaging 20 (2004) 531–537.
[25] R.J. Ordidge, M. Wylezinska, J.W. Hugg, E. Butterworth, F. Franconi, Frequency offset corrected inversion (FOCI) pulses for use in localized spectroscopy, Magn. Reson. Med. 36 (1996) 562–566.